CHROMOSPHERIC HEIGHT AND DENSITY MEASUREMENTS IN A SOLAR FLARE OBSERVED WITH RHESSI

II. *Data Analysis*

MARKUS J. ASCHWANDEN[1], JOHN C. BROWN[2] and EDUARD P. KONTAR[2]
[1]*Lockheed Martin Advanced Technology Center, Solar & Astrophysics Laboratory, Department L9-41, Bldg. 252, 3251 Hanover St., Palo Alto, CA 94304, U.S.A. (e-mail: aschwanden@lmsal.com)*
[2]*Astronomy and Astrophysics Group, Department of Physics and Astronomy, University of Glasgow, Glasgow G12 8QQ, U.K. (e-mail: john@astro.gla.ac.uk)*

(Received 19 July 2002; accepted 15 August 2002)

Abstract. We present an analysis of hard X-ray imaging observations from one of the first solar flares observed with the Reuven Ramaty High-Energy Solar Spectroscopic Imager (RHESSI) spacecraft, launched on 5 February 2002. The data were obtained from the 22 February 2002, 11:06 UT flare, which occurred close to the northwest limb. Thanks to the high energy resolution of the germanium-cooled hard X-ray detectors on RHESSI we can measure the flare source positions with a high accuracy as a function of energy. Using a forward-fitting algorithm for image reconstruction, we find a systematic decrease in the altitudes of the source centroids $z(\varepsilon)$ as a function of increasing hard X-ray energy ε, as expected in the thick-target bremsstrahlung model of Brown. The altitude of hard X-ray emission as a function of photon energy ε can be characterized by a power-law function in the $\varepsilon = 15-50$ keV energy range, viz., $z(\varepsilon) \approx 2.3(\varepsilon/20 \text{ keV})^{-1.3}$ Mm. Based on a purely collisional 1-D thick-target model, this height dependence can be inverted into a chromospheric density model $n(z)$, as derived in Paper I, which follows the power-law function $n_e(z) = 1.25 \times 10^{13}(z/1 \text{ Mm})^{-2.5}$ cm^{-3}. This density is comparable with models based on optical/UV spectrometry in the chromospheric height range of $h \lesssim 1000$ km, suggesting that the collisional thick-target model is a reasonable first approximation to hard X-ray footpoint sources. At $h \approx 1000-2500$ km, the hard X-ray based density model, however, is more consistent with the '*spicular extended-chromosphere model*' inferred from radio sub-mm observations, than with standard models based on hydrostatic equilibrium. At coronal heights, $h \approx 2.5-12.4$ Mm, the average flare loop density inferred from RHESSI is comparable with values from hydrodynamic simulations of flare chromospheric evaporation, soft X-ray, and radio-based measurements, but below the upper limits set by filling-factor insensitive iron line pairs.

1. Introduction

In this paper we measure for the first time hard X-ray source altitudes with the RHESSI spacecraft, which has an unprecedented energy resolution thanks to the germanium-cooled detectors, and thus is expected to provide the most accurate spectral height measurements. The reason is because the observed height distribution of hard X-ray emission, which is a convolution of the electron injection spectrum, the bremsstrahlung cross-section, and the instrumental spatial/energy resolution, can most accurately be modeled for a high energy resolution. We model the spatial distribution of hard X-ray sources observed with RHESSI during the 20

Solar Physics **210:** 383–405, 2002.

February 2002 flare according to the theoretical model of thick-target bremsstrahlung derived in Paper I (Brown, Aschwanden, and Kontar, 2002).

Hard X-ray height limits on the regions of particle acceleration and energy deposition have first been obtained using stereoscopic observations with multiple spacecraft. Kane (1983) found that 95% of the ≈ 150 keV X-ray emission in impulsive flares originates at attitudes $\lesssim 2.5$ Mm, and also 75% of the 100–150 keV emission of gradual flares was found at altitudes of $\lesssim 2.5$ Mm. Brown *et al.* (1983) modeled the height structure of stereoscopically observed flares and found that those with heights of $\lesssim 2.5$ Mm could satisfactorily be explained by the collisional thick-target model (Brown, 1971; Brown and McClymont, 1976) with direct precipitation (no trapping) while hard X-ray emission from occulted flares with height levels of ≈ 25.0 Mm could not be explained with the basic thick-target model. Height measurements of hard X-ray sources have also been obtained by measuring the displacement of hard X-ray source centroids from the reported Hα flare positions. Takakura *et al.* (1986) measured a hard X-ray source height of $h = 7.0 \pm 3.5$ Mm above the neutral line seen in Hα in the 20–40 keV range with *Hinotori*. Matsushita *et al.* (1992) measured the statistical displacement of hard X-ray source centroids to reported Hα flare positions and found heights of $h_{14} = 9.7 \pm 2.0$ Mm for 14–23 keV (*Yohkoh* Lo band), and height differences of $h_{23} - h_{14} = -1.0 \pm 0.3$ Mm for 23–33 keV (M1 band), $h_{33} - h_{14} = -2.0 \pm 0.5$ Mm for 33–33 keV (M2 band), and $h_{53} - h_{14} = -3.2 \pm 0.7$ Mm for 53–96 keV (Hi band). Fletcher (1996) modeled the theoretical energy dependence of the hard X-ray source heights with a numerical Fokker–Planck collisional transport code and found that Matsushita's measurements can be reproduced with loops that have coronal densities between $n_e = 2 \times 10^{10}$ and 3×10^{11} cm^{-3} and half lengths of $L \approx 13$–27 Mm.

In Section 2 we present the data analysis for the case of the 20 February 2002 flare, in Section 3 we discuss comparisons with previous measurements and alternative models, and in Section 4 a summary and conclusions are given.

2. Data Analysis

2.1. Observations

One of the first prominent flares observed with RHESSI occurred on 20 February 2002, 11:06 UT. It was identified as GOES C7-class flare, occurring in NOAA/USAF active region AR 9825. Big Bear Observatory pinpointed the flare location at N16 W80, i.e., $919''$ west and $285''$ north from solar disk center, and classified the sunspots as β/γ Hale configuration. A light curve of the flare observed by RHESSI in the energy band of $\varepsilon = 12$–50 keV is shown in Figure 1 (bottom), binned in time intervals of 4.0 s, which roughly corresponds to the RHESSI spin rate. The actual spin rate of RHESSI was determined by the Photo-Multiplier-Tube Roll Aspect System (PMTRAS) to be $R = 4.3329$ s at the time of the flare

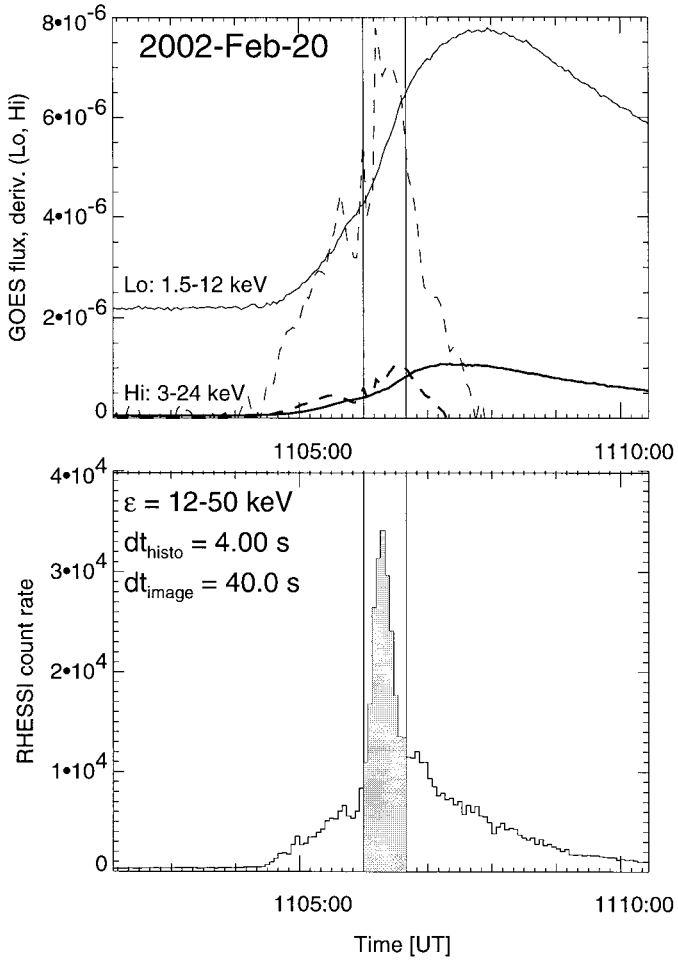

Figure 1. RHESSI (*bottom frame*) and GOES light curves (*top frame*). The GOES light curves are shown for the low-energy (*thin line*) and high-energy channel (*thick line*), along with the time derivative of the GOES flux (*dashed lines*). The RHESSI light curve is binned in steps of $dt_{\rm histo} = 4.0$ s. The time interval $dt_{\rm image} = 40.0$ s used in the images, 16:06:00–16:06:40 UT, is marked with *grey color*.

peak, at 11:06:16 UT. The rotation rate needs to be known with an accuracy of at least 10^{-4} to calibrate the phase of the rotational modulation time profiles properly. Two soft X-ray light curves of the flare observed by GOES are also shown in Figure 1 (top) from the two channels, 1–8 Å (1.5–12 keV) and 0.5–4 Å (3–24 keV), respectively. The time derivative of the soft X-ray light curves (dashed lines in Figure 1, top) matches closely the hard X-ray light curve observed by RHESSI (Figure 1, bottom), as expected from the Neupert effect (e.g., Dennis and Zarro, 1993). For imaging, in different energy ranges we will use the time interval

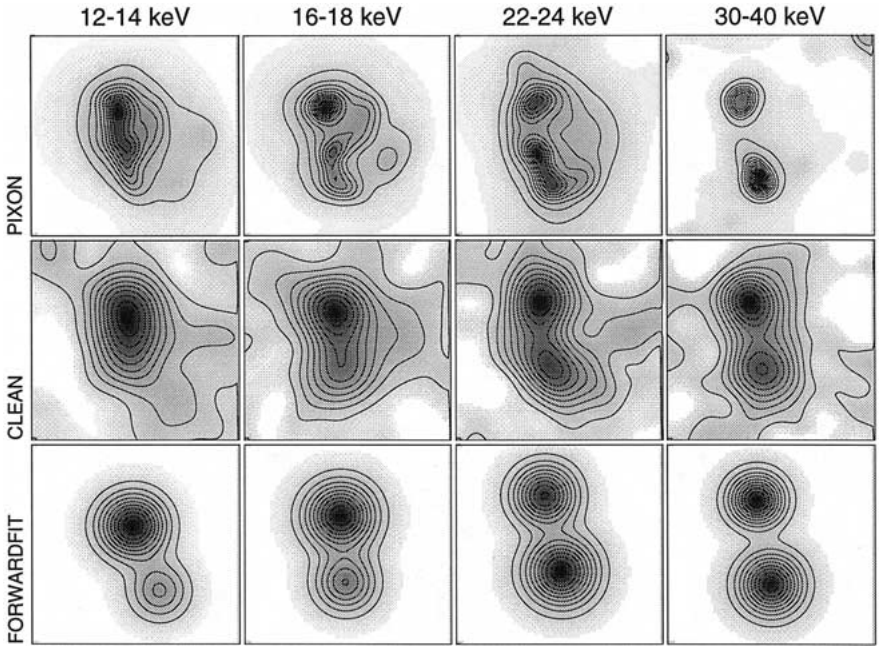

Figure 2. Image reconstructions of the 20 February 2002, 11:06:00–11:06:40 UT flare, observed with RHESSI, using grid Nos. 3–9. The images are reconstructed in four different energy ranges, the lowest showing mainly thermal looptop emission (12–14 keV), while the higher energy ranges (16–18 keV, 22–24 keV, 30–40 keV) display double footpoint sources. Three different imaging algorithms were used: pixon method (*top row*), clean (*middle row*), and forward-fitting of two gaussian sources (*bottom row*). The field of view is in all cases 64″ or 46 Mm. All maps are normalized to the same peak brightness, with contour levels given in increments of 10% of the peak brightness.

of 11:06:00–11:06:40 UT, which extends roughly over 10 RHESSI rotations and encompasses the flare peak (see time interval marked in Figure 1, bottom).

2.2. FLARE LOOP GEOMETRY

In Figure 2 we show RHESSI image reconstructions of the flare during the time interval 20 February 2002 11:06:00–11:06:40 UT in four different energy ranges (12–14, 16–18, 22–24, and 30–40 keV), obtained with three different imaging algorithms, i.e., with the 'pixon', 'clean', and 'forward-fit' algorithms. These image reconstructions have been performed using the RHESSI grids Nos. 3–9, which contain information on spatial scales of 6.8″–183″ (see Table I in Aschwanden *et al.*, 2002b).

Here we discuss the imaging only for RHESSI grids Nos. 3–9 and not for the finest grids Nos. 1–2. This is because the finest grids Nos. 1–2 have not been fully calibrated at the time of writing which, together with the limited photon statistics makes their use rather unreliable for now. Nevertheless we obtain angular measurements of a precision of order that of the finest grids because we are

fitting the centroids of parametric models rather than recovering the full image structure. At the time of image reconstruction (May 2002), the RHESSI software had already implemented (1) the roll-angle aspect solution (PMTRAS), (2) the corrected grid No. 5 calibration, and (3) corrections for small ($\lesssim 100$ ms) data drop-outs due to cosmic-ray hits. A comparison of the three imaging algorithms shows both similarities and significant differences. The clean algorithm iteratively deconvolves a backprojection map with a calculated pointspread function, which has roughly a FWHM of the finest grid with significant modulation ($\approx 7''$ here). The clean images (Figure 2, middle row) contain also a residual map which provides a measure of the data noise. The pixon images were produced, unlike the clean algorithm, by fitting the theoretically calculated modulation time profiles from a pixonized model map to the observed time profiles. In this comparison in Figure 2 they tend to show somewhat sharper source structures and thus reveal some more detailed structures than the clean maps. The forward-fitting maps were produced by fitting the modulation time profiles of a parameterized model map with two gaussian source structures to the observed time profiles. This forwardfit method places all the flux into two locations that represent the best possible approximation to the real flux distribution, under the constraint of the particular parameterizations of 2 circular gaussian sources. The feature that is commonly reproduced by all three algorithms is the double-source structure for energies above 15 keV, while a single-source structure is seen at all lower energies (as imaged in the range of 3–15 keV).

The contours at the half peak flux of the forward-fitting maps are overlaid in Figure 3, for energies of $\varepsilon = 15, 20, \ldots, 45$ keV. Because the centroids of the double gaussians are nearly co-spatial at higher energies, we interpret the two locations as conjugate footpoints of a flare loop (or a compact loop arcade). With forward-fitting, the centroids of the gaussian source structures can be localized more precisely than the angular resolution. This super-resolution, however, hinges on the assumption of a gaussian (or some other few-parameter) source model. For asymmetric sources there would be a possible bias depending on the skewness (3rd-order moment) of the true source distribution. The locations of the two footpoints, as determined from the averaged centroids of the forward-fitted gaussians at high energies ($\gtrsim 40$ keV), are found at the coordinates $X_1, Y_1 = [906.6'', 252.3'']$ and $X_2, Y_2 = [900.9'', 277.0'']$ west and north of Sun center. This yields a midpoint position of $[903.7'', 264.6'']$, a loop baseline of $l = 24.8$ Mm, and an azimuth of $\alpha = 102°$ of the baseline to the east–west direction. If we assume a semi-circular geometry for the flare loop (indicated with dashed line style in Figure 2) we have a loop radius of $r_{\rm loop} = l/2 = 12.4$ Mm. The midpoint between the hard X-ray footpoints corresponds to a location of (N16 W75), close to the Big Bear reported flare position (N16 W80). Because this location is close to the limb, we see essentially the loop plane (assumed vertical) unforeshortened, with $\sin(75°) = 0.96$. Radial distances to Sun center correspond therefore to altitude differences in good approximation.

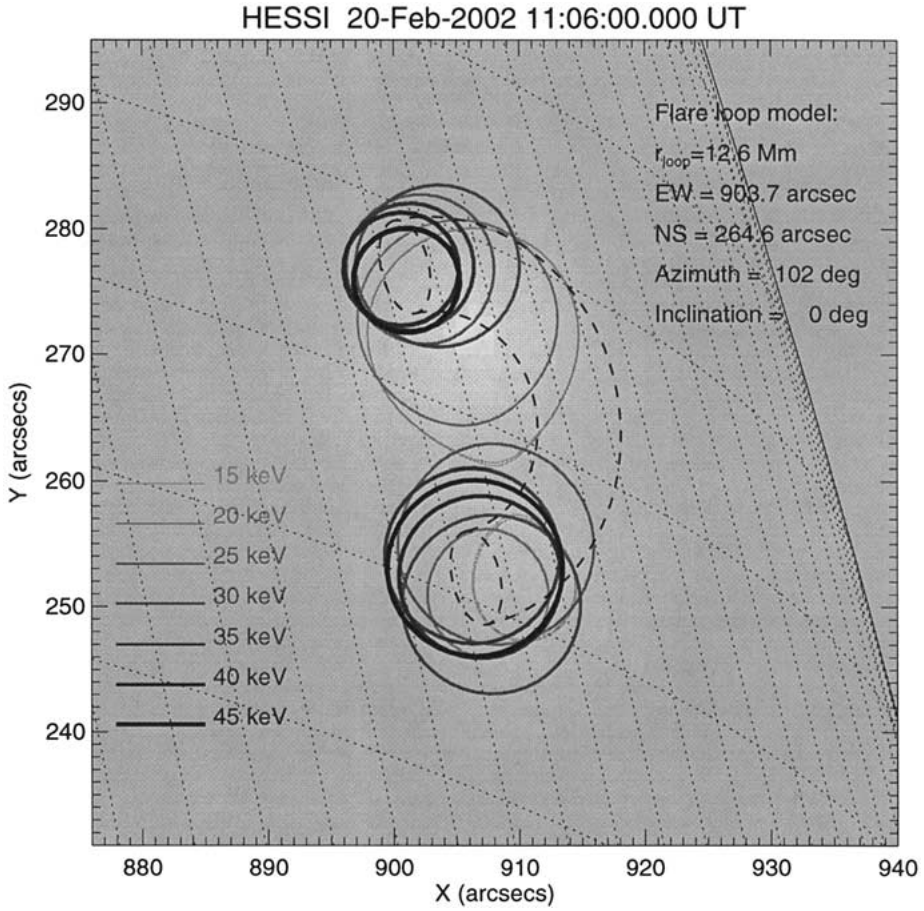

Figure 3. FWHM contours of forward-fit maps overlaid at different energies (15, 20, ..., 45 keV). The greyscale map represents the 15 keV map. A heliographic grid with 1° spacing is overlaid. The *dashed lines* demarcate a flare loop with semi-circular geometry and vertical loop plane. Note that the centroids of the hard X-ray sources systematically increase in altitude with lower energies.

2.3. ALTITUDE MEASUREMENTS OF HARD X-RAY SOURCES

The next step is to measure the radial distances $r(\varepsilon)$ of the hard X-ray footpoint sources from Sun center as a function of energy ε. We reconstructed 68 images with the forward-fitting method in the energy range of $\varepsilon = 3, \ldots, 7$ keV, in steps of 1 keV. The energy widths $\Delta\varepsilon$ of the images were chosen to be wide enough to ensure acceptable image quality, i.e. $\Delta\varepsilon = 2$ keV for energies of $\varepsilon \leq 25$ keV, $\Delta\varepsilon = 4$ keV for energies of 25 keV $< \varepsilon <$ 35 keV, and $\Delta\varepsilon = 10$ keV for energies of $\varepsilon \geq 35$ keV, respectively. From the forwardfit maps we obtain the image coordinates x_i, y_i of the gaussian source centroids (with respect to Sun center). We sort the coordinates of the two gaussian sources into northern (N) and southern (S) sources and determine their distances to Sun center, e.g.,

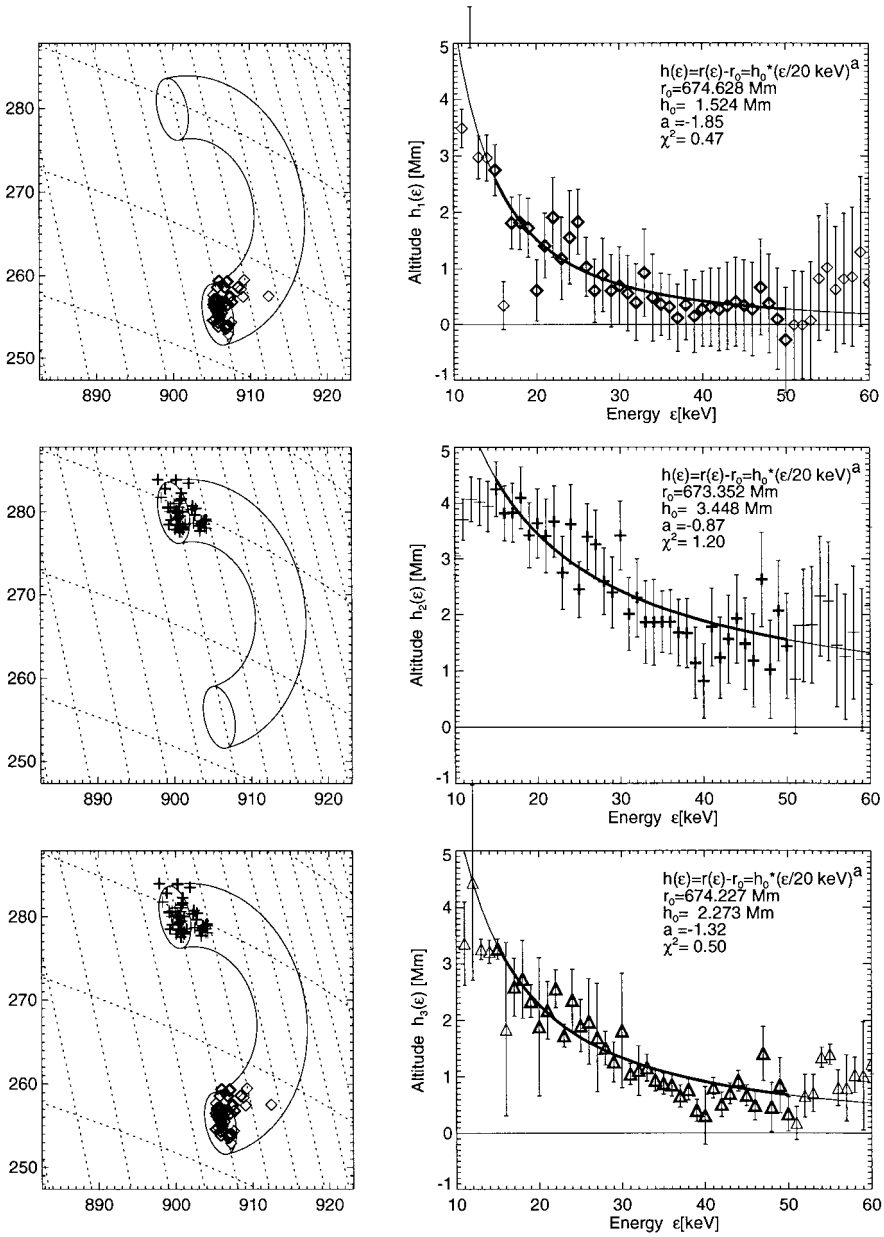

Figure 4. Height measurements of the centroids of the gaussian fits to the hard X-ray sources. The spatial location of the source centroids are shown in the *left side*, the altitudes as functions of energy in the *right panels*. Measurements at the southern footpoint are shown in the *top panels*, at the northern footpoint in the *middle panels*, and combined measurements in the *bottom panel*. The error bars of the height measurements were estimated from Poisson statistics in the cases of single footpoints, or from the differences in the case of combined footpoints. The curves indicate power-law fits, marked with thick linestyle in the energy range of the fit (15–50 keV). The best-fit parameters are also indicated.

$$r(\varepsilon_i) = \sqrt{x_i^2 + y_i^2}. \tag{1}$$

The positions of the source centroids are shown in Figure 4 (with cross symbols for the northern sources in the middle left panel and with diamond symbols for the southern sources in the top left panel in Figure 4). The location of the centroid positions shown in Figure 4 have been rotated by an empirical (energy-dependent) roll angle of $7^\circ/\varepsilon_{\rm keV}$ to correct for a spin rate drift of $\approx 14''/40$ s that is presently not fully accounted for in the imaging software. This roll-angle drift is energy-dependent because the image reconstruction is flux-weighted and the flux at lower energies peaks later than at higher energies (Neupert effect). This roll angle correction places all source locations within a loop diameter of $\approx 5''$) (Figure 4, left panels), but in no way affects the height measurements $r(\varepsilon_i)$ here, because it is strictly in the orthogonal direction.

The measured source altitudes $z(\varepsilon_i) = r(\varepsilon_i) - r_0$ are shown in Figure 4 (right panels), defined by a height difference of the radial distance r to Sun center to a reference height r_0. We choose a power-law function to fit the observed source altitudes $z(\varepsilon)$ as a function of the energy ε,

$$z(\varepsilon) = r(\varepsilon) - r_0 = z_0 \left(\frac{\varepsilon}{20\ {\rm keV}}\right)^{-a}. \tag{2}$$

In the high-energy limit ($\varepsilon \mapsto \infty$) this power-law function yields as asymptotic limit a zero height ($z \mapsto 0$), which we can associate with the solar surface. This power-law function has three free parameters, the source height z_0 at 20 keV, the reference level r_0, and the power-law slope a. We determine these three parameters from a least-square fit (with the Powell minimization method) to the observed values $r(\varepsilon_i)$. We fit only over the energy range 15 keV $< \varepsilon_i <$ 50 keV, which is the energy range that exhibits clear double-footpoint morphology. For the northern footpoint we find the parameters $r_0^N = 674.6$ Mm, $z_0 = 1.5$ Mm, and $a = 1.85$, and for the southern footpoint $r_0^N = 673.4$ Mm, $z_0 = 3.4$ Mm, and $a = 0.87$, respectively. If we average the altitudes from both footpoints (and adjust them to the same reference height) we find $r_0 = 674.2$ Mm, $z_2 = 2.3$ Mm, and $a = 1.32$ (Figure 4, bottom right).

We attempted to estimate the uncertainties σ_r of the height measurements r from the simulations of double footpoint sources in Aschwanden *et al.* (2002b), which scale as a function of the gaussian source width w (in arcsec) and photon count statistics as

$$\sigma_r = w'' \left(\frac{696\ {\rm Mm}}{R_\odot''}\right)\ 10^{-1.27} \left(\frac{10^4}{R\ \Delta t}\right)^{1/2}\ ({\rm Mm}), \tag{3}$$

where $R_\odot = 970.5''$ is the solar radius, R the count rate, and Δt the imaging time interval. These formal error bars are shown in Figure 4 (right top and middle panel), yielding a $\chi^2 = 0.47$ and 1.20, for the power-law height model fit of Equation (2). Another estimate of the systematic uncertainty of height measurements

can be obtained from the difference of heights at the northern and southern location, assuming that the same chromospheric density model holds at both places. Using the half height difference $\sigma_z = |z_N - z_S|/2$ as an estimate of the uncertainty, we find a $\chi^2 = 0.50$ for a model fit to the combined heights $z(\varepsilon) = (z_N + z_S)/2$ (Figure 4, bottom right).

The height dependence $z(\varepsilon)$ can also be fitted with an exponential function or a logarithmic function over this limited range of energy $\varepsilon = 15$–50 keV. We fitted these alternative functions and obtained comparable χ^2-values in the order of unity, so that the data cannot distinguish between these different models. However, a power-law function $z(\varepsilon)$ is analytically (Equation (2)) most convenient and seems to provide reasonable physical limits even beyond the observed parameter range.

2.4. Chromospheric density model

The power-law dependence $z(\varepsilon)$ (Equation (2)) deduced from the observations can be inverted to give,

$$\varepsilon(z) = 20 \left(\frac{z}{z_0} \right)^{-1/a} \text{ (keV)}. \tag{4}$$

This expression can first be inserted into the simple form solution (Equation (7) in Paper I) for the chromospheric density model $n(z)$, after calculating the derivative $\mathrm{d}\varepsilon/\mathrm{d}z$. This yields also a power-law function for the density model $n(z)$,

$$n(z) = n_0 \left(\frac{z}{z_0} \right)^{-b}, \tag{5}$$

with the density constant n_0,

$$\begin{aligned} n_0 &\approx \frac{(20 \text{ keV} \times 1.610^{-9} \text{ erg keV}^{-1})^2}{\text{K}} \left(\frac{1}{a} \right) \left(\frac{1 \text{ Mm}}{z_0} \right) \\ &\approx 1.5 \times 10^{12} \left(\frac{1}{a} \right) \left(\frac{1 \text{ Mm}}{z_0} \right) \text{ (cm}^{-3}\text{)}, \end{aligned} \tag{6}$$

and the power-law slope b,

$$b = 1 + \frac{2}{a}. \tag{7}$$

From the best-fit parameters ($a = 1.32$, $b = 2.52$, $n_0 = 1.14 \times 10^{12}$ cm^{-3}, $z_0 = 2.3$ Mm) to the combined footpoint sources we obtain a chromospheric density model of

$$n(z) \approx 1.14 \times 10^{12} \left(\frac{z}{z_0} \right)^{-2.5} = 9.2 \times 10^{12} \left(\frac{z}{1 \text{ Mm}} \right)^{-2.5} \text{ (cm}^{-3}\text{)}. \tag{8}$$

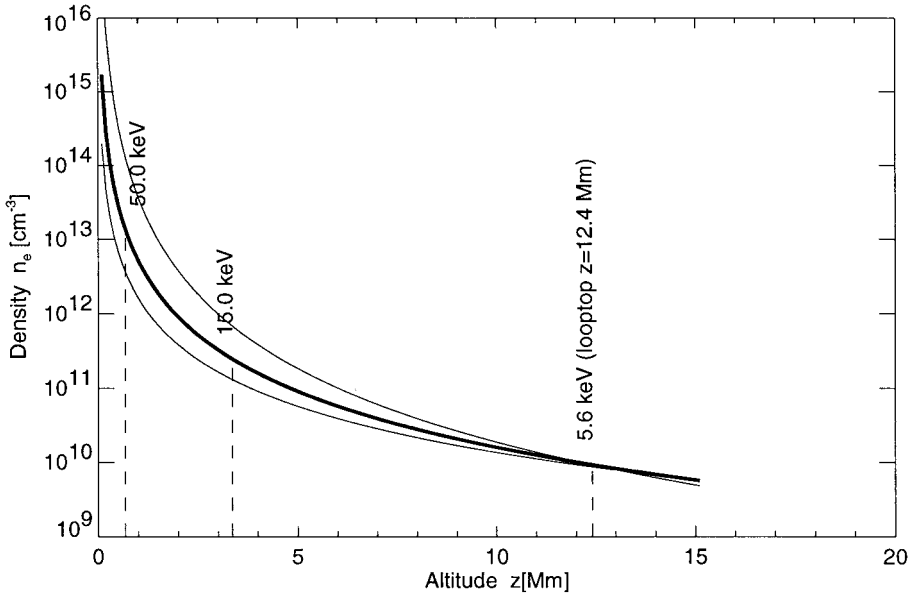

Figure 5. The chromospheric density model $n_e(z)$ resulting from the best fit of the accurate model to the data. The accurate model includes the spectral dependence in terms of Kramer's cross-section (Paper I, Sections 2.4 and 2.5). The densities are a factor of 1.36 lower in the simple model (Paper I, Section 2.3). The thin curve represents the model at the northern and southern loop side, while the thick curve represents the averaged positions. The power-law model is constrained in the height range of $h = 0.7-3.3$ Mm, corresponding to the energy range (15–50 keV) of the fit.

Figure 5 shows the chromospheric density model resulting from the accurate model (including the spectral dependence of $\varepsilon \leq E$ in terms of Kramer's cross-section), which differs only by a density factor of 1.36 from the simple model (with the simplified assumption $z = z(N(\varepsilon)) = z(N = \varepsilon^2/2K)$). In this model, electrons that produce 15–50 keV hard X-rays are stopped at a heights of $z(\varepsilon = 15 \text{ keV}) = 3.4$ Mm and $z(\varepsilon = 50 \text{ keV}) = 0.7$ Mm, respectively.

2.5. HEIGHT FITTING

In Figure 6 we show the observed photon spectrum at the flare peak time, averaged over the time interval of 40 s over which the images were accumulated. This photon spectrum covers the same time interval and energy range of the 68 images reconstructed with forward-fitting. To find γ, δ the spectral fit was performed for the whole source volume with the standard SPEX software adapted for RHESSI in the SSW software. The spectrum can be fitted with a thermal plus a power-law function, as shown in Figure 6. The thermal spectrum that dominates at energies of $\lesssim 15$ keV corresponds to a temperature of $T = 15.3$ MK. Above an energy of $\gtrsim 15$ keV, the nonthermal spectrum dominates, which was fitted with a power-law slope of $\gamma = 3.89$, corresponding to a power-law slope of $\delta = \gamma + 1 = 4.89$

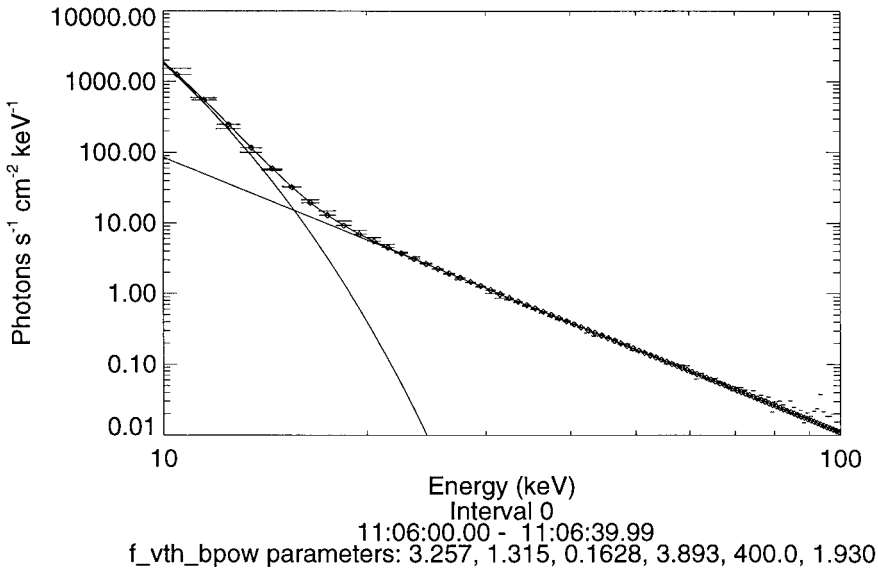

Figure 6. Photon spectrum (photons s^{-1} cm^{-2} keV^{-1}) and spectral fits of a combined thermal and single-power-law spectrum in the energy range of 10–100 keV and time interval 11:06:00–11:06:40 UT. In the range of 20–100 keV, the spectrum can be approximated by a power law with a slope of $\gamma = 3.89$. The thermal spectrum that dominates $\lesssim 15$ keV corresponds to a temperature of $T = 15.3$ MK (or 1.315 keV).

for the electron injection spectrum in terms of the thick-target model. The accurate value of the spectral slope depends on various effects, i.e., (1) the temporal variation during the imaging time interval, (2) the energy range selected for fitting, (3) the spectral model chosen for fitting (e.g., single-power law vs. thermal-plus-power-law function), and (4) the chosen spatial volume (whole source versus single footpoints). By varying all these effects using different image reconstruction methods (CLEAN, MEM-Sato, MEM-Vis) we found a range of $\gamma \approx 3.1$–3.9 for this particular flare time interval, which translates into an uncertainty range of 2.6 for the density scale factor n_0 in the inferred chromospheric density model. This is less than the uncertainty due to the simplifications made in the thick-target model in Paper I.

In order to derive the heights $z(\varepsilon)$ that correspond to the flux maxima of the gaussian fits we have to determine the location $z_{\max}$ of the peaks in the theoretical height distributions $\mathrm{d}I/\mathrm{d}z(\varepsilon, z)$ expressed in terms of incomplete beta functions (Equation (25) and Figures 1 and 2 in Paper I). The flux maxima $z_{\max}(\varepsilon)$ can be determined numerically. We calculate the flux distributions $\mathrm{d}I/\mathrm{d}z(\varepsilon, z)$ for the observationally determined spectral slope $\delta = 4.89$ and the approximate values obtained from the simple model, i.e., $a = 1.32$, $b = 1 + 2/a = 2.5$, $n_0 = 1.14 \times 10^{12}$ cm^{-3}, $N_0 = n_0 z_0/(b-1) = 7.6 \times 10^{20}$ cm^{-2}, and $z_0 = 2.3 \times 10^8$ cm. We then vary the free parameters b and n_0 until we find the best match to the

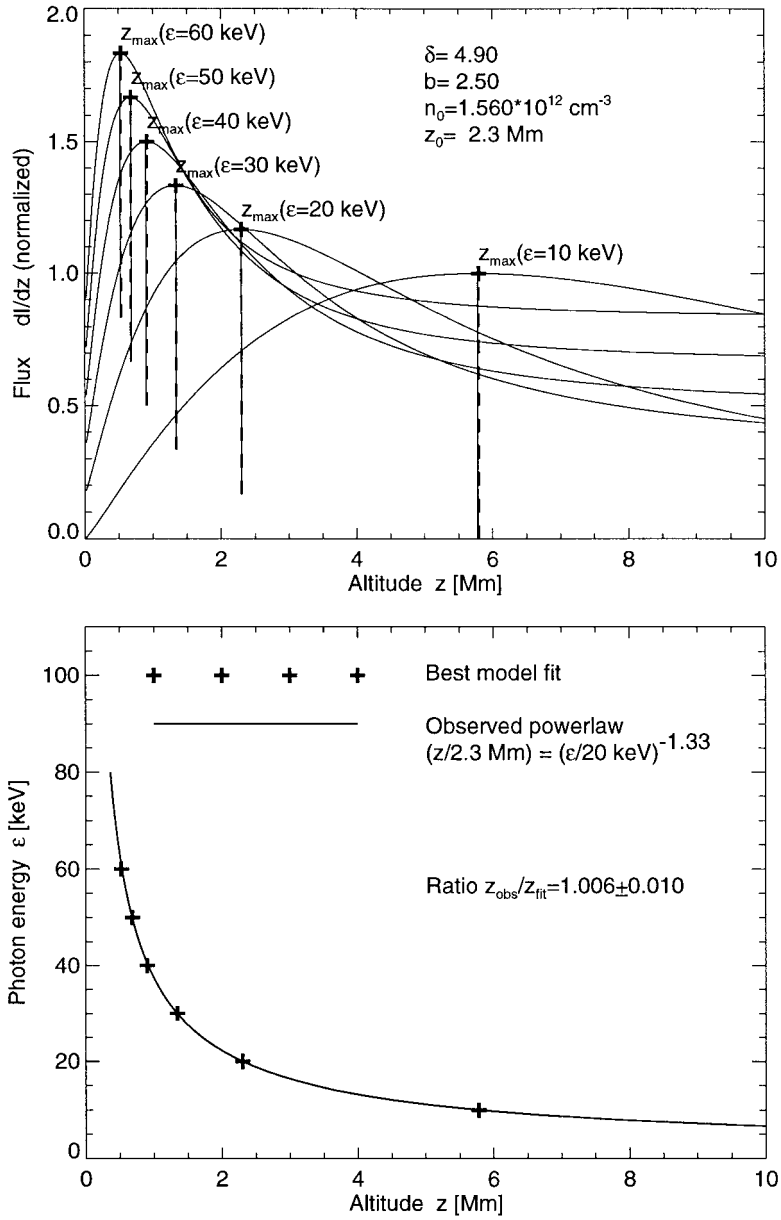

Figure 7. The analytical functions of the energy flux per height range, $\mathrm{d}I/\mathrm{d}z(\varepsilon, z)$ (see Equation (25) in Paper I), for six different energies, $\varepsilon = 10, 20, \ldots, 60$ keV, as a function of the altitude z (*top panel*). The functions are normalized to unity and shifted by 0.1 per energy value to make them visible. The locations $z_{\max}(\varepsilon)$ of these functions are found numerically (marked with a *cross* and a *vertical solid line*). The locations of the observed heights of the gaussian sources are indicated with *vertical dashed lines*, which coincide with the function maxima positions for this best fit. The parameters n_0 and b of the theoretical function have been optimized until the maxima $z_{\max}$ of the theoretical model coincided with the observed heights. The location of the same maxima are also shown as function of energy in the lower panel. The agreement between the model and the best fit amounts to $z_{\mathrm{obs}}/z_{\mathrm{fit}} = 1.006 \pm 0.010$.

observed heights of the gaussian source centroids, which follow approximately the power-law function given in Equation (2), $z_{\rm obs}(\varepsilon) = z_0(\varepsilon/20\ {\rm keV})^{-1.32}$. We find a best fit for the parameters $b = 2.5$ and a density constant $n_0 = 1.56 \times 10^{12}$ cm^{-3}. Thus our best-fit density model is

$$n(z) \approx 1.56 \times 10^{12} \left(\frac{z}{z_0}\right)^{-2.5} = 1.25 \times 10^{13} \left(\frac{z}{1\ {\rm Mm}}\right)^{-2.5}\ ({\rm cm}^{-3}). \tag{9}$$

The display of $\varepsilon(z_{\rm max})$ shown in Figure 7 (bottom panel) illustrates that the best model fit (marked with crosses in Figure 7, determined from the maxima of the theoretical function with the incomplete beta function (see Equation (25) in Paper I), matches the observed power-law function $(z/2.3\ {\rm Mm}) = (\varepsilon/20\ {\rm keV})^{-1.32}$ with an accuracy of $z^{\rm obs}/z^{\rm fit} = 1.006 \pm 0.010$, averaged over the energy range of 10–60 keV. The height distribution $I(z, \varepsilon)$ is shown in graphical form in Figure 7, and as a brightness map in Figure 8. Note that the low-energy emission at $\varepsilon \lesssim 15$ keV is spread over a considerable fraction of the flare loop, while high-energy emission at $\varepsilon \gtrsim 20$ keV is fairly concentrated in chromospheric heights $h \lesssim 2.5$ Mm.

For the best model fit used above with $\gamma = 3.89$ the mono-energetic approximation $\varepsilon \approx E$ (made in the approximate density model of Section 2.3 in Paper I) leads to a density scale value n_0 which is a factor of 1.36 smaller than that for the spectrally corrected value with the (Kramer's) bremsstrahlung cross-section $Q(\varepsilon, E)$. If one uses a higher energy range to estimate γ one gets a larger differential factor between the two methods because for flatter electron spectra more photons are emitted at well below the short-wavelength limit.

3. Discussion

Here we discuss three topics that are relevant to our results: comparison with previous hard X-ray altitude measurements (Section 4.1), comparison of our inferred chromospheric density model with previous chromospheric and coronal density models (Section 4.2), and comparison of our inferred average flare loop density with previous measurements and numerical simulations of the density in the chromospheric evaporation phase (Section 4.3).

3.1. Hard X-ray altitude measurements

Previous altitude measurements of hard X-ray sources have been performed by stereoscopic observations of occulted flares (Kane, 1983), by relative displacements of hard X-ray source centroids from Hα flare positions (Takakura *et al.*, 1986; Matsushita *et al.*, 1992), by displacements above the solar limb (Aschwanden *et al.*, 1999), and in this study by fitting a power-law density model $h(\varepsilon) = r(\varepsilon) - r_0 \sim \varepsilon^{-a}$ to the observed distances $r(\varepsilon)$ from Sun center. Each method

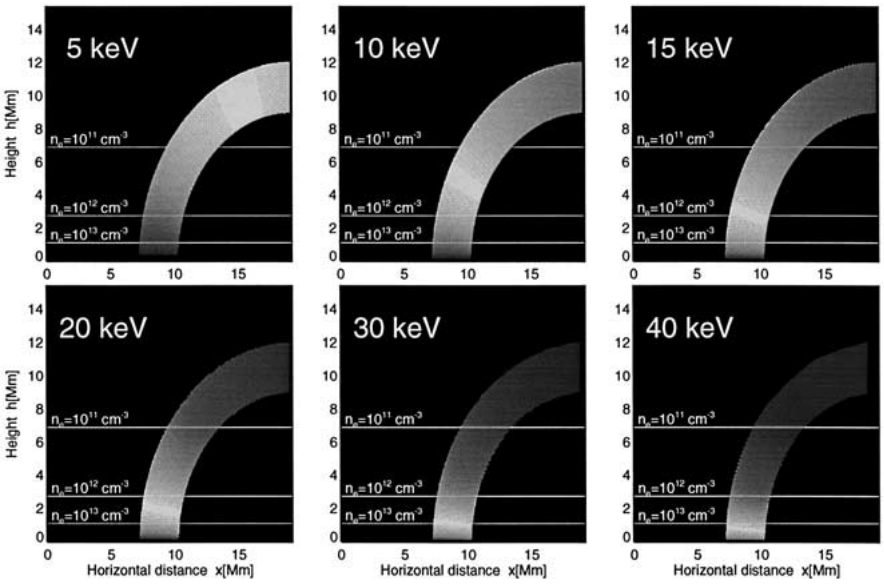

Figure 8. The height distributions $I(z, \varepsilon)$ are computed for $\varepsilon = 5, 10, \ldots, 40$ keV and are represented by brightness maps of the flare loops in different energy bands. The vertical axis represents the height scale h, for a flare loop with a loop radius of 12.4 Mm. The corresponding chromospheric densities n_e are indicated on the *right side*. Note that the brightness distributions of all energies $\varepsilon \gtrsim 20$ keV are fairly concentrated inside the chromosphere (at $h \lesssim 2.0$ Mm), while the $\varepsilon \lesssim 15$ keV emission is spread along the entire flare loop.

has its own systematic errors, which have never been compared in detail. We show a comparison with the previous results in Figure 9. If we plot the reported absolute heights (Figure 9, top), we find that all previously measured altitudes are higher than those measured with RHESSI in this study. The reason for this systematic trend is not obvious, although we expect arbitrary offsets between Hα and hard X-ray flare positions, because the brightest part of the often quite long Hα flare ribbons do not necessarily coincide with the rather concentrated hard X-ray footpoints of flare loops. Also we know that Hα flare positions are reported with typical accuracies of 1 heliographic degree, which corresponds to 12 Mm. In the statistical dataset of Matsushita *et al.* (1992), which contains 92 flare events, the absolute height error was estimated to $\sigma_h = 2.0$ Mm. Even in the highest energy channel (53–93 keV) analyzed by Matsushita *et al.* (1992), a source height of $h_{53} = 6.5 \pm 2.0$ Mm was deduced, which requires a thick-target density of $n_e \approx 10^{13}$ cm^{-3}, which is unlikely to exist at this height (Figure 5), according to standard chromospheric models (Figure 10). Thus, we conclude that most of the previous absolute height measurements have large uncertainties that were not properly accounted for.

A much better agreement is achieved in the relative height measurements of hard X-ray sources at different energies. In Figure 9 (bottom panel) we show the

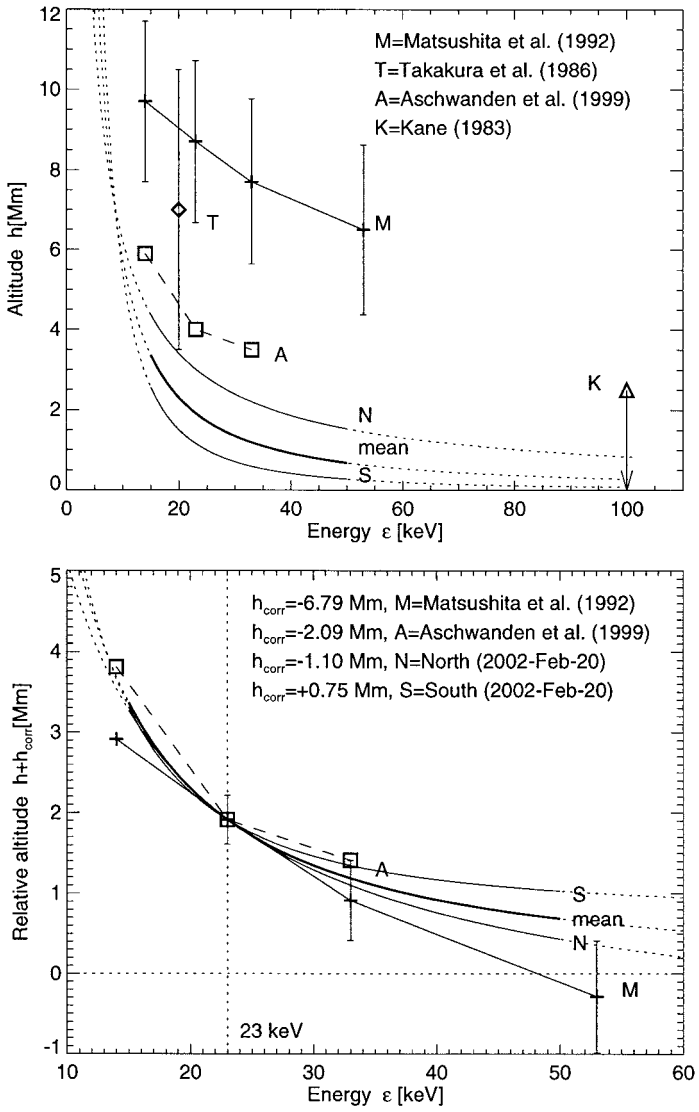

Figure 9. A compilation of reported hard X-ray source heights is shown in the *top panel*, from Kane (1983), Takakura *et al.* (1986), Matsushita *et al.* (1992), and Aschwanden *et al.* (1999), and from this work (N, S, mean). In the *lower panel* we shift the absolute height to a common reference level of $h = 1.9$ Mm at $\varepsilon = 23$ keV. Note that the agreement of relative source heights as function of energy (*lower panel*) agrees much better than the absolute heights (*top panel*).

relative height differences for a common reference height of $h(\varepsilon = 23$ keV)= 1.9 Mm. The required corrections of the reported absolute altitudes are: $h_{\rm corr} = -6.8$ Mm (Matsushita *et al.*, 1992), $h_{\rm corr} - 2.1$ Mm (Aschwanden *et al.*, 1999), and $h_{\rm corr} - 1.1$ Mm and $+ 0.8$ Mm for the north and south footpoints of the 20 February 2002 flare. The relative heights at different energies agree then within $\Delta h \approx \pm 0.5$ Mm over the entire energy range from 10 to 50 keV, all being consistent with a thick-target model with plausible chromospheric densities, even if we allow for the larger values inferred using smaller values of γ. Note, however, that $\Delta h \approx \pm 0.5$ corresponds to almost 2 density scale heights at low chromospheric temperatures, or a factor of 10 uncertainty in n.

3.2. CHROMOSPHERIC DENSITY MODELS

The main new result from this study is that we determine for the first time a chromospheric density model $n_e(h)$ from hard X-ray measurements, enabled by the new capabilities of RHESSI. It is therefore instructive to put our measurements into context with previous chromospheric models. A compilation of a number of chromospheric density models available in literature is shown in Figure 10. Chromospheric and coronal density models are sharply divided by a thin transition region where the temperature rises from the temperature minimum region ($\approx 10\,000$–$20\,000$ K) to coronal temperatures ($T_e \gtrsim 1$ MK). Below the transition region, the plasma is only partially ionized, and thus the electron density n_e is lower than the hydrogen density $n_{\rm H}$. At the transition region, where complete ionization sets in, the neutral hydrogen density $n_{\rm H^0}$ drops then to a very small value, at an altitude of approximately $h \approx 2.0$ Mm (Figure 10). Above the transition region, i.e., at $h \gtrsim 2.0$ Mm, the plasma is fully ionized and the electron density is almost equal to the ion density, i.e., $n_e \approx n_i$. Coronal density models therefore assume $n_e(h) \approx n_i(h)$.

Chromospheric density models have been calculated in great detail based on ion abundance measurements from a larger number of EUV lines, constrained by hydrostatic equilibrium and radiation transfer assumptions (e.g., Vernazza, Avrett, and Loeser, 1973, 1976, 1981; VAL models, see Figure 10), and ambipolar diffusion (Fontenla, Avrett, and Loeser, 1990, 1991; FAL models, see Figure 10). Newer developments include sunspot umbral models (Maltby *et al.*, 1986; Obridko and Staude, 1988), sunspot penumbral models (Ding and Fang, 1989), or stochastic multi-component models with hot flux tubes randomly embedded in a cool medium (Gu *et al.*, 1997), all shown in Figure 10. At coronal heights, i.e., at $h \gtrsim 2.0$ Mm, an average quiet sun density model was computed by Gabriel (1976), based on the expansion of the magnetic field of coronal flux tubes that line up with the boundaries of the supergranule convection cells. The geometric expansion factor and the densities at the lower boundary computed from chromospheric models then constrains coronal densities, which fall off exponentially with height, in isothermal fluxtubes with hydrostatic equilibrium. This yields electron densities of $n_e \approx 10^9$ cm^{-3} at the

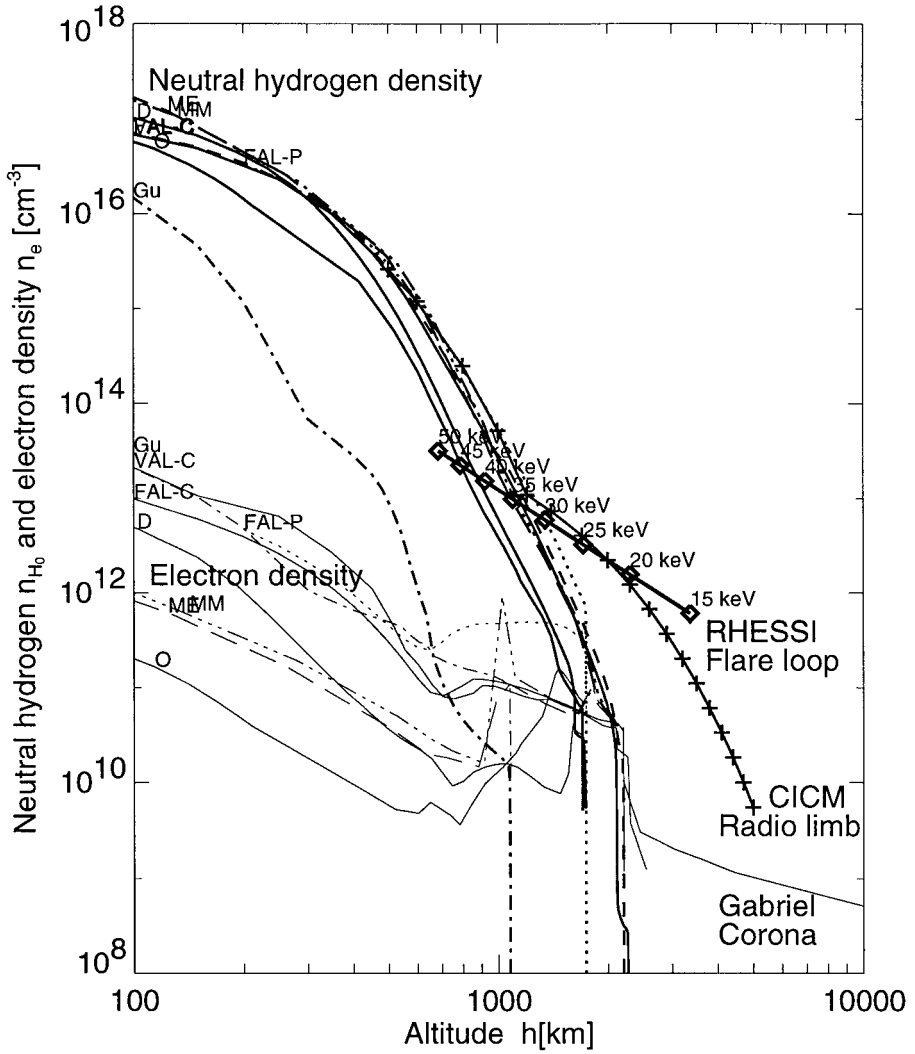

Figure 10. A compilation of chromospheric and coronal density models: VAL-C = Vernazza, Avrett, and Loeser (1981), model C; FAL-C = Fontenla, Avrett, and Loeser (1990), model C; FAL-P = Fontenla, Avrett, and Loeser (1990), model P; Gu = Gu *et al.* (1997); MM = Maltby *et al.*, 1986), model M; ME = Maltby *et al.* (1986), model E; D = Ding and Fang (1989); O = Obridko and Staude (1988); Gabriel = Gabriel (1976), coronal model; CICM = Caltech Irreference Chromospheric Model, radio sub-millimeter limb observations (Ewell *et al.*, 1993), RHESSI flare loop (this work).

coronal base in quiet-Sun regions (Gabriel, 1976), as shown in Figure 10. These hydrostatic models in the lower corona, however, have been criticized because of the presence of dynamic phenomena such as spicules, which contribute in the statistical average to an extended chromosphere. The spicular extension of this dynamic chromosphere has been probed with high-resolution measurements of the Normal

Incidence X-Ray Telescope (NIXT) (Daw, DeLuca, and Golub, 1995) as well as with radio submillimeter observations during a total eclipse (Ewell *et al.*, 1993). At radio wavelengths, the opacity of the chromosphere is due to free-free emission, which can be modeled straightforwardly from radio brightness temperature measurements at the limb. Using the radio limb height measurements at various mm and sub-mm wavelengths in the range of 200–3000 μm (Roellig *et al.*, 1991; Horne *et al.*, 1981; Wannier, Hurford, and Seielstad, 1983; Belkora *et al.*, 1992; Ewell *et al.*, 1993), an empirical Caltech Irreference Chromospheric Model (CICM) was established, which fits the observed limb heights between 500 km and 5000 km in a temperature regime of $T = 4410$ K to $T = 7500$ K (Ewell *et al.*, 1993), shown in Figure 10. We see that these radio limb measurements yield electron densities that are 1–2 orders of magnitude higher in the height range of 500–5000 km than predicted by hydrostatic models (VAL, FAL, Gabriel, 1976), which was interpreted in terms of the dynamic nature of spiculae (Ewell *et al.*, 1993). Comparing now our RHESSI measurements, which mainly probe the total neutral and ionised hydrogen density that governs the bremsstrahlung and the total bound and free electron density in the collisional energy losses, with the free electron density $n_e(h)$ inferred from the radio-based measurements of free-free emission, we see a remarkably good agreement, between the two density profiles in the height range of $h \approx 1000$–3000 km. The RHESSI-inferred densities in the hot parts of the flare loop ($\gtrsim 3000$ km) exceed the radio-inferred densities, probably due to the process of chromospheric evaporation, which we discuss in the next subsection.

3.3. CHROMOSPHERIC EVAPORATION

The collisional degradation of high-energy electrons precipitating during the impulsive flare phase heats up the chromospheric plasma and drives an upflow of heated plasma that fills the flare loops (Brown, 1973), most visible in the emission measure increase in soft X-rays, a scenario dubbed *chromospheric evaporation* (e.g., see reviews by Bornman, 1999 and Antonucci *et al.*, 1999). Hydrodynamic simulations of this particle-driven chromospheric heating process yield typical densities of $n_e \approx 10^{11}$ cm^{-3} for the upflowing plasma (e.g., Mariska, Emslie, and Li, 1989; Mariska, 1995; Hori *et al.*, 1997, 1998). Slightly higher densities can be obtained by increasing the energy flux (of precipitating electrons and ions), but radiative loss becomes so efficient that not much more density can be pumped into the flare loops (Mariska, private communication).

We can compare the RHESSI-inferred densities with the values obtained from chromospheric evaporation models by averaging the density model $n(z)$ over a volume that corresponds to the hot flare loop segment, as seen in soft X-rays. Because the density is rapidly decreasing with height, we have to be careful where we assume the lower height limit of the hot flare plasma. According to the chromospheric models shown in Figure 10, the lower limit of the hot flare loop segment could be anywhere between $h \gtrsim 1000$ km and $h \lesssim 5000$ km, where dense cool spicular

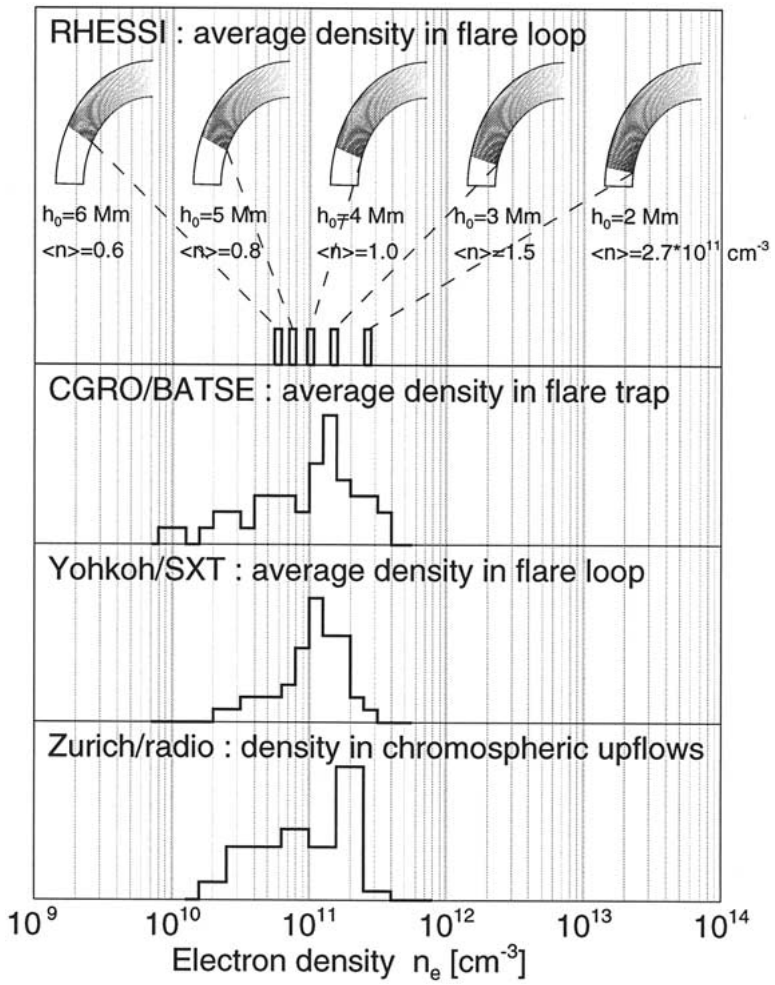

Figure 11. A comparison of average flare loop densities, obtained from RHESSI, CGRO/BATSE, *Yohkoh*/SXT, and Zürich radio measurements. The flare loop densities are obtained from RHESSI by averaging the thick-target density model over a loop segment between h_0 and the top, calculated for $h_0 = 2, 3, 4, 5, 6$ Mm, with a loop height of $r_0 = 12.4$ Mm (indicated as shaded loop segments at the top). The resulting densities vary from $\langle n \rangle = 0.6 \times 10^{11}$ cm^{-3} to $\langle n \rangle = 2.7 \times 10^{11}$ cm^{-3}. Densities in the flare loop trap are inferred from CGRO/BATSE (*second panel*) in terms of trapping time delays interpreted as collisional deflection times (Aschwanden *et al.*, 1997). Densities in soft X-ray-bright flare loops have been determined from *Yohkoh*/SXT (*third panel*) by measuring the emission measure and loop diameters (Aschwanden *et al.*, 1997). Densities in chromospheric upflows were measured from Zürich radio measurements of slowly-drifting cutoffs at decimetric frequencies interpreted in terms of free-free opacity changes at the upflow fronts (Aschwanden and Benz, 1997).

material resides (CICM model). The average density is therefore, if we integrate the power-law function of our chromospheric density model (Equation (5)) over a loop segment of $h_0 < h < r_0$ (neglecting the curvature near the flare loop top, where the contributions to the average density are lowest anyway),

$$\langle n \rangle \approx \frac{\int_{h_0}^{r_0} n(s)\,\mathrm{d}s}{\int_{h_0}^{r_0} \mathrm{d}s} \approx n_0 \frac{z_0}{1.5(r_0 - h_0)} \left[\left(\frac{h_0}{z_0} \right)^{-1.5} - \left(\frac{r_0}{z_0} \right)^{-1.5} \right]. \tag{10}$$

Our flare loop of the 20 February 2002 flare has a height of $r_0 = 12.4$ Mm. If we vary the lower height of the hot flare loop segment between $h_0 = 2000$ km and $h_0 = 6000$ km, we obtain average densities between $\langle n \rangle = 0.6 \times 10^{11}$ cm^{-3} and $\langle n \rangle = 2.7 \times 10^{11}$ cm^{-3} (illustrated in Figure 11, top panel). Thus, these average densities of the hot flare loop plasma are fully compatible with values obtained from hydrodynamic simulations, which typically yield $\langle n \rangle \approx 10^{11}$ cm^{-3}. This is of course in line with the simpler estimate that one needs a stopping depth of $N \approx 10^{20}$ to stop a typical beam electron which, divided by loop length of 10^9 cm, yields $\langle n \rangle \approx 10^{11}$ cm^{-3}.

It is also interesting to compare these values with other methods. In Figure 11 we show comparisons with three different methods. From CGRO/BATSE data one can measure energy-dependent time delays that are associated with electron time-of-flight propagation as well as with trapping times. Interpreting the trapping times in terms of collisional deflection times, $\tau^{\rm defl}(E) = 0.95 \times 10^8 (E_{\rm kev}^{3/2}/n_e)(20/\ln \Lambda)$, one obtains average trap densities of $10^{10} \lesssim n_e \lesssim 4 \times 10^{11}$ cm^{-3} (Figure 11, second panel), with an average of $n_e^{\rm trap} = 10^{11.1 \pm 0.3}$ (Aschwanden *et al.*, 1997). A second method is to measure the soft X-ray emission measure $EM = \int n_e^2(z)\mathrm{d}z \approx n_e^2 w$ and the flare loop widths w. This method yields density values in a range of $2 \times 10^{10} < n_e < 3 \times 10^{11}$ cm^{-3} in a sample of 78 flares simultaneously observed with *Yohkoh*/SXT and CGRO (Aschwanden *et al.*, 1997). A third method can be performed with radio observations of slowly-drifting frequency cutoffs of decimetric emission at the plasma frequency, which has been interpreted as opacity change at the interface of chromospheric evaporation fronts (Aschwanden and Benz, 1997). This method yields densities in the range of $2 \times 10^{10} < n_e < 3 \times 10^{11}$ cm^{-3} (Figure 11, bottom panel). All three methods yield comparable densities with an average of $n_e \approx 10^{11}$ cm^{-3}, but could be higher if there are filling factors involved. In this context it is highly interesting to note what highest electron densities in solar flares have been determined from density-sensitive line pairs, i.e., Fe XXI and Fe XXII, which are not sensitive to the filling factor (but see Almleaky, Brown, and Sweet, 1990, for a critical treatment). These highest densities were found at $n_e = 2\text{–}3 \times 10^{12}$ cm^{-3}, with a maximum of $n_e \approx 10^{13}$ cm^{-3}

(Phillips *et al.*, 1996). Therefore, our hard X-ray-inferred average flare loop densities ($n_e \approx 2\text{–}8 \times 10^{11}$ cm^{-3}) agree very well with the three other methods based on the assumption of unity filling factor, but also agree with the upper limits set by filling factor-independent density measurements at the footpoints of our hard X-ray-inferred density model.

4. Summary and Conclusions

We fitted the theoretical model $I(z, \varepsilon)$ derived in Paper I to gaussian forward fits of RHESSI observations, where the height z above the solar surface was measured over an energy range of $\varepsilon = 15\text{–}50$ keV for a limb flare (20 February 2000). We found the following:

(1) The height of hard X-ray footpoint sources has an energy dependence that can be approximated by a power-law function, i.e., $z(\varepsilon) \approx 2.3(\varepsilon/20\,\text{keV})^{-1.32}$ Mm in the $\varepsilon = 15\text{–}50$ keV energy range for a spectral fit with $\gamma = 3.9$, though the absolute density scale could be up to a factor of ≈ 2.6 higher due to uncertainties ($\gamma \approx 3.1\text{–}3.9$) in the spectral fitting procedure.

(2) The best fit of the analytical model $I(z, \varepsilon)$ to the data is consistent with a chromospheric density model of $n_e(h) = 1.25 \times 10^{13}(z/1\text{ Mm})^{-2.5}$ cm^{-3}, for a spectral fit with $\gamma = 3.9$, though the absolute scale depends somewhat on the choice of energy range in spectral fitting.

(3) The unprecedented energy resolution of RHESSI yields a value of the flare plasma temperature, i.e., $T \approx 15$ MK, which dominates the observed photon spectrum at energies of $\varepsilon \lesssim 15$ keV, while the high-energy hard X-ray emission at $\varepsilon \gtrsim 15$ keV is nonthermal (or at least non-isothermal). Hard X-ray emission in the energy range of $\varepsilon = 15\text{–}20$ keV is produced by thick-target bremsstrahlung from larger fractions of the flare loop (see Figure 8), at heights of $h \approx 2.5\text{–}12.4$ Mm and densities of $n_e \approx 10^{11}\text{–}10^{12}$ cm^{-3}, while higher energy emission of $\varepsilon = 20\text{–}50$ keV originates from thick-target bremsstrahlung in chromospheric heights of $h \approx 500\text{–}2500$ km and densities of $n_e \approx 10^{12}\text{–}10^{14}$ cm^{-3}.

(4) Previous altitude measurements of hard X-ray sources are systematically higher than the RHESSI-inferred altitudes at the same energies, probably suffering from insufficient energy and spatial resolution of previous hard X-ray imagers. The relative altitude differences as a function of energy, however, agree well with the RHESSI measurements.

(5) The chromospheric density model inferred from RHESSI roughly agrees with the ion densities of previous chromospheric density models based on optical/EUV spectroscopy, at altitudes of $h \approx 500\text{–}1000$ km. At coronal heights, the RHESSI density model comes closest to the '*spicular extended chromospheric model*' inferred from radio sub-mm limb observations. Such spicules are indicative of a highly dynamic chromosphere, and have densities lying several orders of magnitude above quiet-Sun chromosphere/coronal models based on hydrosta-

tic equilibrium. The evaporative upflow in flares is a more extreme form of such deviation from hydrostatic conditions.

(6) The average flare loop densities obtained from the RHESSI measurements, $\langle n \rangle \approx 0.6\text{–}3 \times 10^{11}$ cm^{-3}, are fully comparable with other flare loop density measurements (assuming unity filling factor), $\langle n \rangle \approx 0.2\text{–}3 \times 10^{11}$ cm^{-3}, though substantially lower than the estimates of the highest densities present as measured by density-sensitive line ratios (cf., Almleaky, Brown, and Sweet, 1989) which reach $\langle n \rangle \approx 10^{12}\text{–}10^{13}$ cm^{-3}.

Our measurements and quantitative modeling have demonstrated that the Brown (1971) collisional thick-target model seems to be a pretty good description of the hard X-ray height structure for reasonable target density models. If one accepts the purely collisional thick-target model then RHESSI provides useful data to constrain the density model in the chromospheric and coronal parts of flare loops. The hard X-ray inferred density models have moreover the advantage that they determine spatial mean densities averaged over any highly localized regions, independent of filling factors. Also, no assumption on hydrodynamic equilibrium is needed, which is a restriction in most density models based on optical/EUV spectroscopy. Accurate measurements of chromospheric density are also important to modeling coronal loop oscillations regarding Alfvénic wave propagation, wave leakage, and associated damping mechanisms (e.g., Aschwanden *et al.*, 2002a). Future energy-dependent height measurements with RHESSI hopefully will also help constrain particle propagation all the way back to the acceleration regions. Some final caveats that add additional uncertainties to our density inversion method are discussed in Paper I, concerning non-collisional energy losses, pitch-angle distributions, partial target ionization, and return current losses.

Acknowledgements

We thank Tom Metcalf for providing the pixon maps in Figure 2, Bart DePontieu for the digitized chromospheric data shown in Figure 10, and John Mariska for helpful information on hydrodynamic simulations of chromospheric evaporation. Also we thank the RHESSI team for extensive software support, useful tutorials and data analysis training workshops, and very helpful personal advice by many software team members. Support for this work was provided by the NASA SMEX grant NAS5-98033 through University of California, Berkeley (sub contract SA2241-26308PG) and by UK PPARC Standard and Visitor Grants.

References

Almleaky, Y., Brown, J. C., and Sweet, P. A.: 1989, *Astron. Astrophys.* **224**, 328.

Antonucci, E., Alexander,D., Culhane, J. L., DeJager, C., MacNeice, P., Somov, B. V., and Zarro, D. M.: 1999, in K. T. Strong, J. L. R. Saba, B. M. Haisch, and T. Schmelz (eds.), *The Many Faces*

of the Sun, A Summary of the Results from NASA's Solar Maximum Mission, Springer-Verlag, Berlin, p. 331.
Aschwanden, M. J.: 2002, *Space Sci. Rev.* **101**, 1.
Aschwanden, M. J. and Benz, A. O.: 1997, *Astrophys. J.* **480**, 825.
Aschwanden, M. J., Bynum, R. M., Kosugi, T., Hudson, H. S., and Schwartz, R. A.: 1997, *Astrophys. J.* **487**, 936.
Aschwanden, M. J., Fletcher, L., Sakao, T., Kosugi, and Hudson, H.: 1999, *Astrophys. J.* **517**, 977.
Aschwanden, M. J., DePontieu, B., Schrijver, C. J., and Title, A.: 2002a, *Solar Phys.* **206**, 99.
Aschwanden, M. J., Schmahl, E. J. and the RHESSI Team, 2002b, *Solar Phys.* (this volume).
Belkora, L., Hurford, G. J., Gary, D. E., and Woody, D.: 1992, *Astrophys. J.* **400**, 629.
Bornmann, P. L.: 1999, in K. T. Strong, J. L. R. Saba, B. M. Haisch, and J. T. Schmelz (eds.), *The Many Faces of the Sun, A Summary of the Results from NASA's Solar Maximum Mission*, Springer-Verlag, Berlin, p. 301.
Brown, J. C.: 1971, *Solar Phys.* **18**, 489.
Brown, J. C.: 1972, *Solar Phys.* **26**, 441.
Brown, J. C.: 1973, *Solar Phys.* **32**, 227.
Brown, J. C. and MacKinnon, A. L.: 1985, *Astrophys. J.* **292**, L31.
Brown, J. C. and Emslie, A. G.: 1988, *Astrophys. J.* **331**, 554.
Brown, J. C., and McClymont, A. N.: 1976, *Solar Phys.* **49**, 329.
Brown, J. C., Carlaw, V. A., Cromwell, D., and Kane, S. R.: 1983, *Solar Phys.* **88**, 281.
Brown, J. C., Aschwanden, M. J., and Kontar, E. P.: 2002, *Solar Phys.*, this volume (Paper I).
Daw, A., DeLuca, E. E., and Golub, L.: 1995, *Astrophys. J.* **453**, 929.
Dennis, B. R. and Zarro, D. M.: 1993, *Solar Phys.* **146**, 177.
Ding, M. D. and Fang, C.: 1989, *Astron. Astrophys.* **225**, 204.
Ewell, M. W. Jr., Zirin, H., Jensen, J. B., and Bastian, T. S.: 1993, *Astrophys. J.* **403**, 426.
Fletcher, L.: 1996, *Astron. Astrophys.* **310**, 661.
Fontenla, J. M., Avrett, E. H., and Loeser, R.: 1990, *Astrophys. J.* **355**, 700.
Fontenla, J. M., Avrett, E. H., and Loeser, R.: 1991, *Astrophys. J.* **377**, 712.
Gabriel, A. H.: 1976, *Phil. Trans. Roy. Soc. (London)* **A281**, 339.
Gu, Y., Jefferies, J. T., Lindsey, C., and Avrett, E. H.: 1997, *Astrophys. J.* **484**, 960.
Hori, K., Yokoyama, T., Kosugi, T., and Shibata, K.: 1997, *Astrophys. J.* **489**, 426.
Hori, K., Yokoyama, T., Kosugi, T., and Shibata, K.: 1998, *Astrophys. J.* **500**, 492.
Horne, K., Hurford, G. J., Zirin, H., and DeGraauw, Th.: 1981, *Astrophys. J.* **244**, 340.
Kane, S. R.: 1983, *Solar Phys.* **86**, 355.
Maltby, P., Avrett, E. H., Carlsson, M., Kjeldseth-Moe, O., Kurucz, R. L., and Loeser, R.: 1986, *Astrophys. J.* **306**, 284.
Mariska, J. T.: 1995, *Astrophys. J.* **444**, 478.
Mariska, J. T., Emslie, A. G., and Li, P.: 1989, *Astrophys. J.* **341**, 1067.
Matsushita, K., Masuda, S., Kosugi, T., Inda, M., and Yaji, K.: 1992, *Publ. Astron. Soc. Japan* **44**, L89.
Obridko, V. N. and Staude, J.: 1988, *Astron. Astrophys.* **189**, 232.
Phillips, K. J. H., Bhatia, A. K., Mason, H. E., and Zarro, D. M.: 1996, *Astrophys. J.* **466**, 549.
Roellig, T. L., Becklin, E. E., Jefferies, J. T., Kopp, G. A., Lindsey, C. A., Orrall, F. Q., and Werner, M. W.: 1991, *Astrophys. J.* **381**, 288.
Takakura, K., Tanaka, K., Nitta, N., Kai, K., and Ohki, K.: 1986, *Solar Phys.* **107**, 109.
Vernazza, J. E., Avrett, E. H., and Loeser, R.: 1973, *Astrophys. J.* **184**, 605.
Vernazza, J. E., Avrett, E. H., and Loeser, R.: 1976, *Astrophys. J. Suppl.* **30**, 1.
Vernazza, J. E., Avrett, E. H., and Loeser, R.: 1981, *Astrophys. J. Suppl.* **45**, 635.
Wannier, P. G., Hurford, G. J., and Seielstad, G. A.: 1983, *Astrophys. J.* **264**, 660.